

Effect of (001) and (111) epitaxial strain on *Pnma* Perovskite oxides

Amartyajyoti Saha,^{1,2} Turan Birol¹

¹*Department of Chemical Engineering and Materials Science, University of Minnesota and*

²*School of Physics and Astronomy, University of Minnesota*

With recent advances in strain engineering and its widespread applications, it is becoming increasingly important to understand the effect of biaxial strain on the most common structural phase of perovskites – the orthorhombic *Pnma* structure. In this work, by using a combination of group theory and first principles density functional theory, we study the effect of biaxial strain on (001) and (111)-oriented CaTiO₃, SrSnO₃ and SrZrO₃ films. We observe manifestly different behaviors depending on the strain orientation, with common trends emerging between different materials. In addition to many different structural phases observed in individual compounds before, we identify a transition between two different phases with the same space group name (*P2₁/c*) but different symmetries in (111)-strained materials. We also find that allowing the relaxation of the out-of-plane monoclinic angles, often ignored in first principles studies, lead to significant stabilization of certain phases and is essential to correctly determine the structural ground state.

I. INTRODUCTION

Biaxial strain, applied on thin films by growing them on lattice mismatched substrates, is a commonly used strategy to modify properties of perovskites and related materials [1, 2]. For example, strain engineering has significant potential to improve the performance and stability of halide perovskite solar cells [1, 3, 4]. It has also been used to tune the emission wavelength of perovskite-based light emitting diodes [5, 6]. A large body of strain engineering work is also focused on perovskite oxide thin films, and their dielectric and ferroelectric properties [7–10].

Most perovskite oxides have one more more structural distortions that make them deviate from the cubic high-symmetry reference structure. By far the most common distortion is the oxygen octahedral rotations that emerge due to the small size and hence under-bonding of the *A*-site cations in *ABO₃* [11, 12]. The octahedral rotations around different cubic axes can have different magnitudes and patterns, which leads to many different space group symmetries [13–15]. The octahedral rotations can also couple with and give rise to other interesting phenomena, such as metal insulator transitions or improper ferroelectricity, which can often be controlled by strain since octahedral rotations often couple with strain strongly [16–18].

More than half of all oxide perovskites have the same oxygen octahedral rotation pattern, shown as $a^-a^-c^+$ in Glazer notation [14], which leads to the orthorhombic space group *Pnma* also observed in the prototypical CaTiO₃ [19]. When under strain, different *Pnma* perovskites stabilize different phases. For example CaTiO₃ attains a polar space group [20], whereas SrSnO₃ is shown to stabilize the tetragonal *I4/mcm* phase under compressive strain [21]. While there are a large number of first-principles studies on individual compounds, an overarching study of biaxially strained *Pnma* perovskites that compares the trends in different compounds and different strain directions is missing to date to the best of our knowledge. In particular, most of the studies on biaxi-

ally strained perovskites focus on (001) films, and first principles work on (111) *Pnma* perovskites is not common. This is despite the fact that there are many exciting theoretical predictions in these systems [22, 23] and a growing number of (111)-oriented thin films grown by MBE or pulsed laser deposition; for example, SrFeO_{2.5} [24], PbTiO₃ [25], SrTiO₃ [26], SrVO₃ [27], various nickelates [28–30] and most recently KTaO₃ [31] have been grown with (111) orientation.

In this work, we use first principles density functional theory to study the structural evolution of three different *Pnma* perovskites under biaxial strain. As three distinct examples, we consider CaTiO₃ [19], SrZrO₃ [32] and SrSnO₃ [33] with Goldschmidt tolerance factors 0.846, 0.861, and 0.873 respectively. Despite having very different *B*-site cations, all three of these perovskites have the *Pnma* symmetry at room temperature, and undergo a series of structural phase transitions to become cubic (*Pm $\bar{3}m$*) at high temperature [33–35]. In order to capture different symmetry states induced by different strain directions, we go beyond the commonly studied (001) films by considering (111) films as well. By considering many possible rotation patterns and structural phases, and projecting the structures obtained from DFT on irreducible representations (irreps) of the space group, we obtain some general trends regarding the effect of strain on the crystal structure in *Pnma* perovskites. Some of our results include that (i) compressive (001) strain increases the octahedral rotation tendencies around the out-of-plane strongly, whereas tensile strain has a relatively mild effect on rotations around in-plane axes, (ii) as a result of this and the competition between the ferroelectric polarization and octahedral rotations, tensile (001) strain is more conducive to ferroelectricity than compressive strain, and (iii) (111) thin films don't develop ferroelectric instabilities and phases as easily as the (001) films, since the shear-like strain due to the expansion or compression of the (111) planes is more favorably accommodated by changing the out-of-plane spacing of atomic layers, rather than the emergence of a polarization. We also show (iv) the presence of a transition be-

tween two nonpolar phases with different symmetry but the same space group name under (111) strained films, and that (*v*) relaxing the monoclinic angle between the out-of-plane axis and the in-plane ones in biaxial relaxations can be important in finding the correct structural ground state.

This paper is organized as follows: In Sec. II, we introduce the details of our computational methods. In Sec. III A, we discuss the common structural instabilities in the $Pnma$ structure. In Sec. III B and Sec. III C, we discuss the relative stability of different structures and the effect of biaxial strain on the rotation irreps under (001) and (111) strain, respectively. We compare the similarities and differences between the (001) and (111) strain in Sec. IV. We conclude with a summary in Sec. V.

II. METHODS

First-principles density functional theory calculations were performed with the revised Perdew-Burke-Ernzerhof generalized gradient approximation for solids (PBEsol) using the Vienna *ab initio* simulation package (VASP) [36–39]. Each of the perovskite structure was obtained from a $2 \times 2 \times 2$ supercell of the relaxed cubic ABO_3 perovskite structure. Different phases were obtained by applying appropriate rotation to the BO_6 octahedra within the supercell. Afterwards, the supercells were biaxially strained on a rigid square grid and the magnitude and angle of the out-of-plane vector, along with the internal coordinates were relaxed. The orientation of the biaxially strained structures are shown in Fig. 1. The supercells were rotated such that the (001) ((111)) plane is normal to the z Cartesian coordinate. The source code of VASP was modified to set the stress components on the $x - y$ plane to zero. This allowed for out-of-plane longitudinal and shear stress components to relax the magnitude and direction of the z axis with the $x - y$ plane, along with the internal coordinates.

In order to study the relaxed structures, Crystallographic Information Files (CIF) were generated for each structure using FINDSYM [40, 41]. The CIF files were analysed to obtain irreps of each unstable mode with ISODISTORT [42, 43]. The order parameters of the Landau Free energy were obtained with INVARIANTS [44, 45]. The Bilbao Crystallographic Server was used as a reference for group theory tables [46]. Crystal structure visualization was carried out using the VESTA software [47].

Phonon calculations were performed using the *direct method* as implemented in the PHONOPY package [48] on a $3 \times 3 \times 3$ supercell. Born charges were obtained from the primitive cell on a $16 \times 16 \times 16$ Γ centered k -point grid.

DFT calculations were performed on a Γ centered Monkhorst-Pack grid [49] of $4 \times 4 \times 4$ k -points, unless otherwise stated, with a 500 eV energy cutoff for the plane wave basis. Spin-orbit coupling was not included since

Compound	Relaxed structure volume (\AA^3)	Lattice constant (\AA)
CaTiO ₃	220.9	3.808
SrSnO ₃	265.5	4.049
SrZrO ₃	274.2	4.092

TABLE I. Relaxed volumes of the 4 f.u. unitcells of $Pnma$ perovskites, and the corresponding pseudo-cubic lattice parameters calculated by the cube root of a quarter of the cell volumes. These lattice constants are used as the definition of 0% strain.

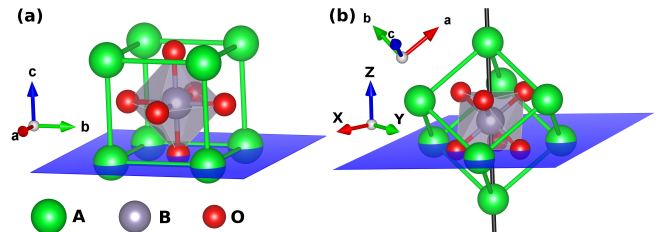


FIG. 1. (a) Cubic perovskite structure under (001) epitaxial strain. We relax the magnitude and direction of c -axis while keeping the ab plane on a rigid square grid. (b) Cubic perovskite structure under (111) epitaxial strain. The Z -axis is parallel to the black line through the B site. We fix the structure on a rigid square grid along XY plane and relax the magnitude and direction of Z -axis.

we found that it did not generate significant qualitative differences. Biaxial strain is measured with respect to the cube root of the computed volume per formula unit of the relaxed $Pnma$ structure, as shown in Table I.

III. RESULTS AND DISCUSSION

A. Structural Instabilities and Related Phases

In this section, we give an overview of important types of structural distortions present or can emerge in $Pnma$ perovskites. These structural distortions can be labelled with the irreducible representations (irreps) of the space group, which enables predicting the space groups of various lower symmetry phases, as well as the form of the Landau free energy expansions. The most common instabilities present in the cubic phase of perovskite oxides are the in-phase and out-of-phase octahedral rotations that transform as the M_2^+ and R_5^- irreps, shown in Fig. 2(c) and 2(f). These rotations are denoted by the ‘+’ and ‘-’ superscripts in the Glazer notation [14], and in perovskites with small tolerance factors (i.e. small A-site cations) their combination with the $a^- a^- c^+$ pattern leads to the orthorhombic structure with the $Pnma$ space group.

The presence of a substrate also breaks the symmetries of the perovskite thin films. In this study, we do not consider interface effects which create a dipole field and directly break the inversion symmetry at the substrate-

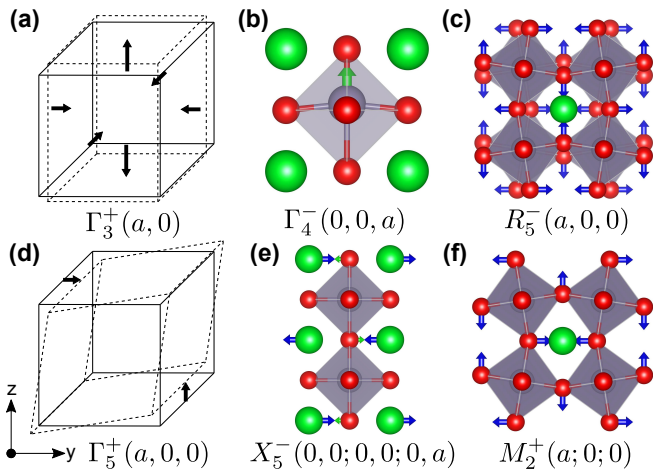


FIG. 2. Prominent structural distortions and corresponding irreps present in $Pnma$ perovskites. (a) Normal strain that keep the cell volume constant transforms as Γ_3^+ . (b) Ferroelectric polarization can simply be represented by the displacement of the B -site cation, which transforms as Γ_4^- . (c) R_5^- is the irrep for the out-of-phase octahedral rotation. (d) Shear strain transforms as Γ_5^+ . (e) X_5^- is an antipolar A -site displacement and (f) M_2^+ is the irrep for the in-phase octahedral rotations.

film interface. We also ignore any ‘substrate imprinting’ effects, which can lower the symmetry of a film further as a result of the structural details of the substrate [18]. In other words, we consider a ‘strained bulk’ configuration, and focus only on strain, which can also be represented by space group irreps. In a cubic material, there are three symmetry inequivalent strain terms: (1) The volume change Γ_1^+ , which is one-dimensional and corresponds to the trace of the strain tensor, (2) the normal strain Γ_3^+ , which is two-dimensional and corresponds to the traceless diagonal part of the strain tensor (Fig. 2(a)), and (3) the shear strain Γ_5^+ , which is three-dimensional and corresponds to the off-diagonal components of the strain tensor (Fig. 2(d)). The biaxial strain conditions we consider are nonzero magnitudes of Γ_3^+ and Γ_5^+ for (001) and (111) strains respectively, and they reduce the cubic $Pm\bar{3}m$ symmetry down to tetragonal $P4/mmm$ and rhombohedral $R\bar{3}m$. Table II shows the space groups obtained by the combination of common octahedral rotation patterns with these types of strain.

In addition to the octahedral rotations, perovskites under strain often develop polar instabilities even if they are centrosymmetric (and hence nonpolar) when unstrained. Polarization transforms as the 3D Γ_4^- irrep of the cubic reference structure (Fig. 2(b)). Including the combination of polarization with octahedral rotations and different strain components leads to a large number of possible symmetries listed in Table III. Additionally, the coexistence of M_2^+ and R_5^- rotations can induce many other types of displacements (secondary order parameters) that transform as different irreps. Perhaps the most important one of these displacements is an anti-polar dis-

Rotation Pattern	S.G. (Bulk)	S.G. (001)-strained	S.G. (111)-strained
$a^0 a^0 a^0$	$Pm\bar{3}m$	$P4/mmm$	$R\bar{3}m$
$a^0 a^0 c^-$	$I4/mcm$	$I4/mcm$	$C2/c$
$a^- a^- c^0$	$Imma$	$Imma$	$C2/c$
$a^0 b^- b^-$	$Imma$	$C2/m$	$C2/c$
$a^- a^- a^-$	$R\bar{3}c$	$C2/c$	$R\bar{3}c$
$a^- a^- b^-$	$C2/c$	$C2/c$	$C2/c$
$a^- a^- b^+$	$Pnma$	$Pnma$	$P2_1/c$
$a^+ b^- b^-$	$Pnma$	$P2_1/m$	$P2_1/c$

TABLE II. List of nonpolar space groups considered in this study, obtained by the combinations of octahedral rotations in perovskites, and different strain directions.

placement of the A -site cations which transform as the X_5^- irrep shown in Fig. 2(e). This mode is discussed in length especially in the context of hybrid improper ferroelectricity [50, 51], but it does not lower the symmetry further in perovskites.

B. Phase diagram under (001) strain

Biaxial strain applied in the (001) plane by means of fixing the a and b correct pseudocubic lattice constants equal, and the angle between them to 90° transforms as the $\Gamma_3^+(a, 0)$ irrep, and reduces the cubic perovskite structure to the tetragonal structure with $P4/mmm$ symmetry. To explore the relative stability of the structures described in Table II under (001) strain, we plot the energy gain with respect to the $P4/mmm$ (strained-cubic) structure in Fig. 3. For simplicity, we only show the ground state candidate structures’ energies in this figure, and other phases’ energies are presented in the supplementary information [52].

Not surprisingly, all three compounds display multiple different structural phases as a function of strain. While the energy gain with respect to the $P4/mmm$ structure without any octahedral rotations is always of the order of multiple meV/f.u. (formula unit), there are regions where the two lowest lying states are very close in energy. It is therefore possible that the structural phase is very sensitively dependent on temperature or even quantum fluctuations at zero temperature. Since DFT cannot directly reproduce these fluctuations, we ignore this possibility, as well as a possible phase separation to accommodate strain better, and focus on the lowest energy phases in the remainder of this paper.

As shown in Fig. 3, SrSnO_3 remains nonpolar within the considered range of strain ($\pm 4.5\%$). Under tensile strain, the $Pnma$ structure of SrSnO_3 has the lowest energy. This is the same space group as the bulk compound, and it has the axis with the in-phase rotations (c) aligned with the normal to the substrate plane. At lower values of tensile, as well as zero and compressive strain values, this is no longer the preferred configuration. Below $\sim 0.5\%$ strain, $P2_1/m$ becomes the lower

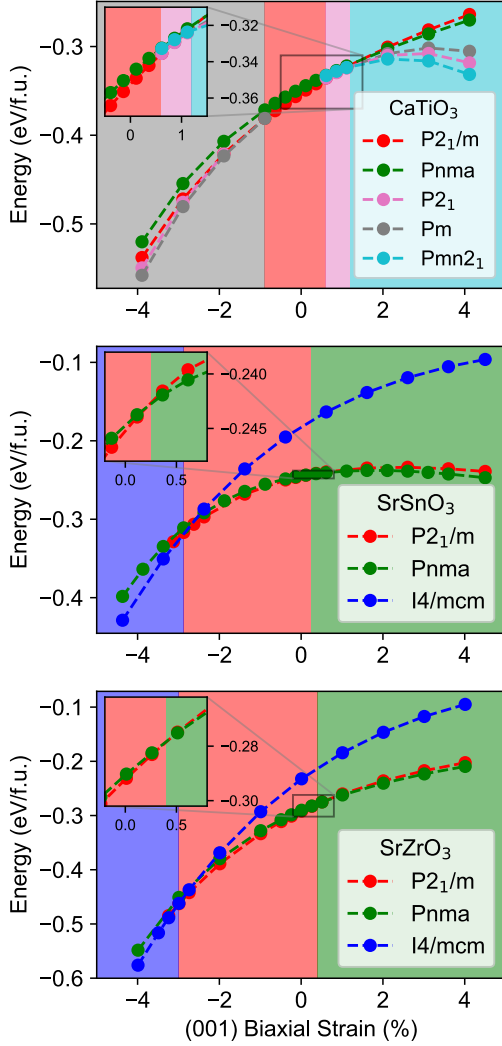


FIG. 3. Phase diagram of $Pnma$ Perovskites under (001) epitaxial strain. For each strain value, relative energy stability is reported with respect to the reference $P4/mmm$ structure at the same strain value. Negative (positive) values represent compressive (tensile) (001) biaxial strain. The dotted lines are guides to the eye.

energy structure. In this structure, the rotation pattern is $a^+b^-c^-$, so it can be considered as the same rotation pattern as bulk, but the in-phase rotation axis is aligned in-plane. The reason that this is the lowest energy structure even at zero strain, instead of the $Pnma$ structure, is that the zero strain boundary conditions are different from the bulk zero stress boundary conditions. In particular, the two in-plane axes are fixed to be normal to each other and have the same lattice parameter $a = b$, which is not the case in the orthorhombic $Pnma$ space group in bulk. Also, the zero strain value of a is determined by the cube root of a quarter of the volume of the bulk $Pnma$ structure's unit cell, which is not exactly equal to the pseudo-cubic lattice constant in any direction in the bulk compound. At large compressive

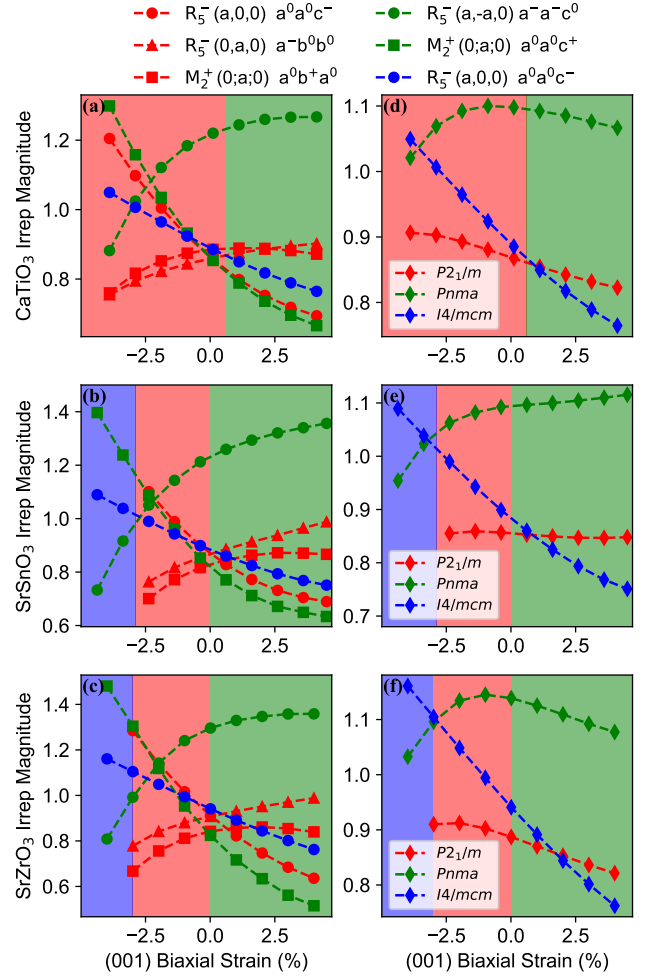


FIG. 4. Amplitudes of the octahedral rotation irreps, R_5^- and M_2^+ , of the stable phases as a function of (001) strain. Panels (a), (b) and (c) show the individual components while panels (d), (e) and (f) show the average rotation magnitude over three axes. The red, green and blue colors correspond to the irreps present in $P2_1/m$, $Pnma$ and $I4/mcm$, respectively. The out-of-plane rotation magnitude increases with increasing (001) compressive strain. This rotation competes with ferroelectric instability, making polarization harder in the compressive region. In the tensile region, the rotation magnitudes do not change significantly.

strain, around $\sim -3\%$, there is another transition from $P2_1/m$ to $I4/mcm$. This is a single tilt system $a^0a^0c^-$, which is commonly observed in perovskites under compressive strain to accommodate shorter in-plane $B-O$ bond-lengths better. Consistent with earlier studies [53], there is no ferroelectric phase in this rather wide strain range. This can be explained by the fact that $SrSnO_3$ has a large B -site cation (Sn) that doesn't exhibit significant hybridization between its conduction band minimum (Sn- s orbitals) and the oxygen- p orbitals, unlike most proper ferroelectric transition metal oxides [54–56].

Interestingly, the phase diagram of $SrZrO_3$ is quali-

tatively identical to SrSnO_3 , despite the fact that Zr is a transition metal ion, and SrZrO_3 has a strong ferroelectric instability in its phonon spectrum in the cubic phase [52, 57]. This ferroelectric instability is suppressed by the octahedral rotations in SrZrO_3 , as is observed in some other $Pnma$ perovskites, and this compound remains nonpolar in the whole strain range we considered ($\pm 4\%$).

CaTiO_3 has a very similar phonon spectrum to SrZrO_3 in the cubic high-symmetry structure, as discussed in Ref. [57]. It too hosts a polar instability in its parent cubic phase that gets suppressed by the octahedral rotations. However, unlike zirconates, ferroelectricity in titanate perovskites is quite common. BaTiO_3 is a prototypical ferroelectric, and both the quantum-paraelectric SrTiO_3 and antiferromagnetic EuTiO_3 are driven to room temperature ferroelectricity under $\sim 1\%$ tensile strain commonly imposed by DyScO_3 substrates [58–60]. Even the layered variants of SrTiO_3 , the $\text{Sr}_{n+1}\text{Ti}_n\text{O}_{3n+1}$ Ruddlesden-Poppers have been shown to undergo ferroelectric transitions under strain [61, 62]. Molecular beam epitaxy-grown thin films of CaTiO_3 are observed to become ferroelectric under strain [20, 63], as predicted by DFT [64].

Our DFT-predicted strain phase diagram of (001)-strained CaTiO_3 is rife with polar phases, as shown in Fig. 3. Around zero strain, biaxially strained CaTiO_3 is in nonpolar $P2_1/m$ phase with the $a^+b^-c^-$ rotation pattern. Under about 1% compressive strain, it undergoes a (second order allowed) phase transition to the polar Pm phase, which arises from polarization of the $P2_1/m$ structure in the out-of-plane direction. Even though this phase is predominantly polarized in the out-of-plane direction, since it is monoclinic, there also exists a small in-plane polarization component. In the tensile region, the $P2_1/m$ phase undergoes another second order-allowed phase transition to the polar $P2_1$ phase, which has an in-plane polarization of the $P2_1/m$ structure, at around 0.5% strain. At around 1% tensile strain, there is a first order phase transition to $Pmn2_1$ phase, which arises from in-plane polarization of $Pnma$ structure. Interestingly, we find that the space group of the bulk compound, $Pnma$ is not realized at any strain value in thin films because of the different boundary conditions for CaTiO_3 .

A pattern that is common in these three $Pnma$ perovskites is that under tensile strain, they have the $a^-a^-c^+$ octahedral rotation pattern, and hence the $Pnma$ or its in-plane polar subgroup in the tensile region; whereas they have the $a^+b^-c^-$ rotation pattern and either $P2_1/m$ or its out-of-plane polar subgroup under compressive (001) strain. In Fig. 4, we show the magnitudes of different components of the octahedral rotations decomposed into the R_5^- and M_2^+ irreps. A trend that is evident is that the rotations around the out-of-plane axis increase rapidly under increasing compressive strain in both the $Pnma$ or the $I4/mcm$ space group. This is not a surprising observation, since this sign of strain decreases the $B\text{-O}$ bond-length, which can be increased

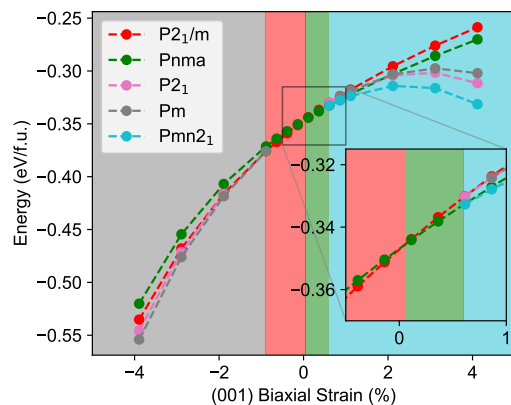


FIG. 5. Phase diagram of CaTiO_3 under (001) biaxial strain without relaxing the monoclinic angles the c axis makes with the biaxial grid.

back by the larger octahedral rotation angle that it holds under $Pnma$ (and even the metastable $P2_1/m$) structure as well.

In passing, we underline the importance of relaxing the monoclinic angle that the out-of-plane lattice vectors make with the in-plane ones in biaxial strain calculations. Especially for small strain values, this angle does not differ much from 90° , and is often assumed to be constant for simplicity. However, especially in regions where multiple phases are close in energy, this angle can make a difference. In Fig. 5, we show the phase diagram of CaTiO_3 without the monoclinic angle relaxed. When the monoclinic angle is not relaxed, the orthorhombic $Pnma$ phase is favored, and it is stabilized in a narrow strain range under small tensile strain, as opposed to the results in Fig. 3(c). This observation signifies the importance of relaxing the monoclinic angle to obtain the correct ground state.

C. Phase diagram under (111) strain

In this section, we consider (111) films. We impose the (111) strain in a way similar to the (001) strain by building a $2 \times 2 \times 2$ supercell of the cubic perovskite structure, changing and fixing the lattice vectors' components on the (111) plane, and relaxing all the other degrees of freedom after applying various octahedral rotation to the BO_6 unit. The strain on the (111) plane corresponds to a shear and transforms as the Γ_5^+ irrep, reducing the symmetry to rhombohedral $R\bar{3}m$. As a result, we use the $R\bar{3}m$ structure as reference and obtain the energies of other structures, with octahedral rotations, with respect to the reference $R\bar{3}m$ structure of equal strain.

Note that while a single lattice parameter (the length of the c -axis) is relaxed on a common (001) strain calculation without any structural distortions besides strain, the (111) strain calculation relax the length of the lattice vector along the $[111]$, which can involve both a change

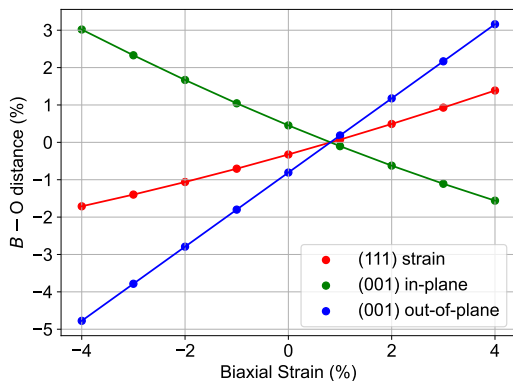


FIG. 6. The $B-O$ distance as a function of biaxial strain for cubic CaTiO_3 . The red, green and blue lines correspond to the $\text{Ti}-\text{O}$ distances under (111) strain (rhombohedral $R\bar{3}m$) and (001) strain (orthorhombic $P4/mmm$ with two inequivalent $\text{Ti}-\text{O}$ distances). The lines meet at a point where the structure is cubic and changes in $\text{Ti}-\text{O}$ distance is in reference to the this structure.

of the rhombohedral angle or the lattice parameter in the rhombohedral structure. In other words, for a cubic perovskite without structural distortions, the (111) strain boundary conditions leave two degrees of freedom as free parameters, as opposed to a single free parameter under the (001) strain boundary conditions. This makes it easier for the compound to accommodate bond lengths without reducing symmetry. This point is illustrated in Fig. 6, which shows the $\text{Ti}-\text{O}$ bond length in CaTiO_3 with no octahedral rotations or polarization under strain. The relaxed structure under different values of (111) strain has its $\text{Ti}-\text{O}$ bond lengths remain equal to each other and depend on strain at a rate of $\lesssim 0.4$ (red line). The (001) strain, on the other hand, leads to two unequal in-plane and out-of-plane bond lengths, which change at rates of ~ -0.6 and ~ 1.0 respectively (green and blue lines). As a result of this degree of freedom, it is likely harder to create new strong instabilities via (111) strain compared to (001) strain. The phonon dispersions of CaTiO_3 , shown in Fig. 7 for 0% and $\mp 4\%$ strain, supports this expectation: While there are some changes in the phonon spectrum, even this large amount of strain doesn't make a dramatic difference in the nature or frequency of the strongest instabilities, which remain the octahedral rotational instabilities.

The phase diagram under (111) strain is shown in Fig. 8. SrZrO_3 realize two different phases under opposite signs of strain, both with $P2_1/c$ symmetry. (Note that this symmetry is obtained trivially when $Pnma$ perovskites are placed under a (111) strain as shown in Tables II and III.) We find that although these two states have the same space group name, they are distinct structures with different directions for the primary M_2^+ and R_5^- order parameters, as well as different induced secondary order parameter irreps. They also have different origin and bases with respect to the parent $Pm\bar{3}m$ struc-

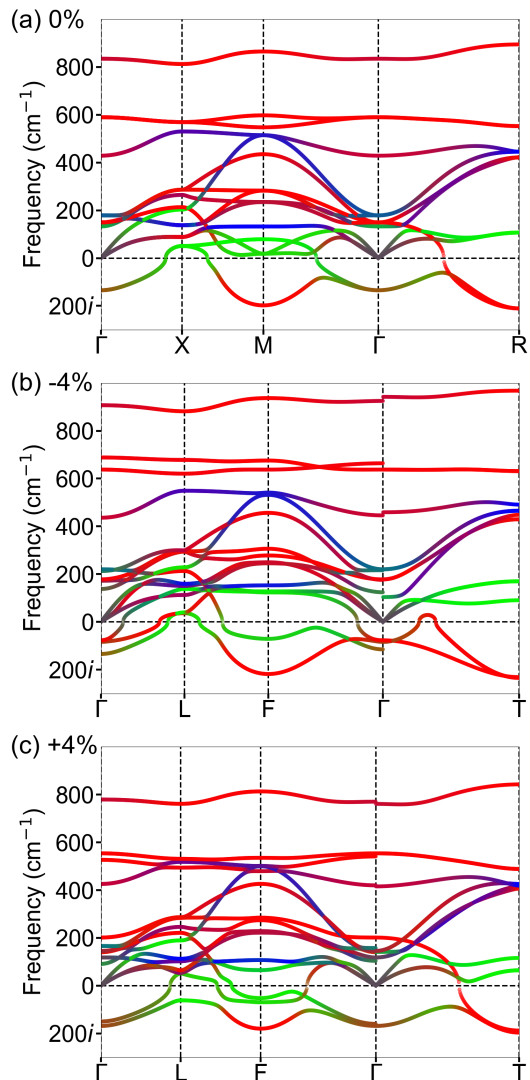


FIG. 7. Phonon dispersions of CaTiO_3 for (a) unstrained cubic structure, and (111)-strained structures with $R\bar{3}m$ symmetry at (b) -4% and (c) $+4\%$ strain. The colors denote the atomic displacement magnitude for Ca (green), Ti (blue) and O (red). We compare the phonon dispersion along related k -points $\Gamma = (0, 0, 0)$, $X = (0.5, 0, 0) = L$, $M = (0.5, 0.5, 0) = F$ and $R = (0.5, 0.5, 0.5) = T$ between the cubic and rhombohedral structures.

ture. Hence, the transition at $\sim 0\%$ strain is not an isostructural transition, despite the *name* of the spacegroup remaining the same. We denote the two phases with spacegroup $P2_1/c$ as Phase A in the compressive region and Phase B in the tensile region. In Fig. 9 and the supplementary information [52], we show a decomposition of both phases into the structural distortions they host. While there is a complex list of many distortions with different irreps in both structures, a distinguishing feature, for example, is the presence of small amplitude secondary order parameters R_2^- and M_2^- in Phase B.

SrSnO_3 also has only the same two phases and a phase transition between them near $\sim 0\%$ strain. However,

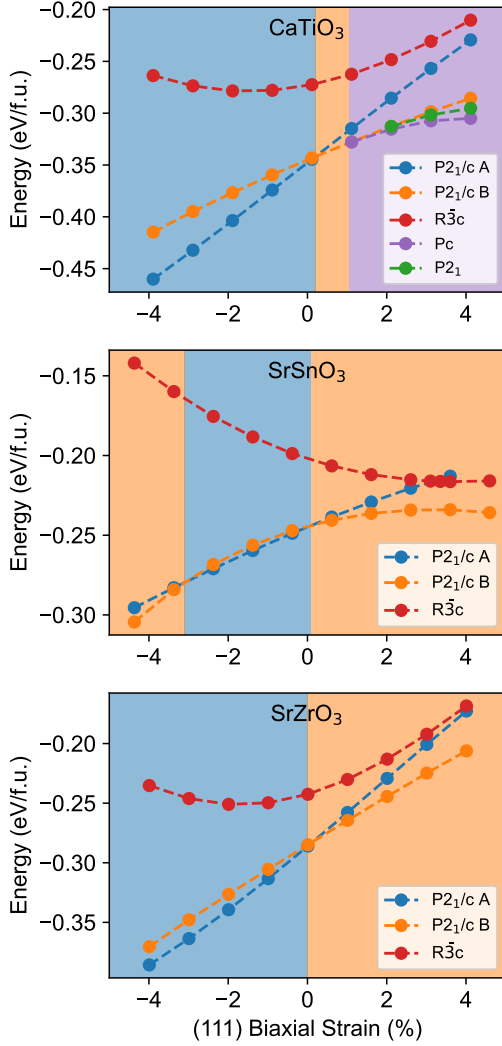


FIG. 8. Phase diagram of $Pnma$ Perovskites under (111) epitaxial strain. For each strain value, relative energy stability is computed with respect to the reference $R\bar{3}m$ structure at the same strain value. Negative (positive) values represent compressive (tensile) (111) biaxial strain. The dotted lines are guides to the eye. The phase diagram is dominated by two distinct structures, both having the $P_{21/c}$ symmetry.

interestingly, the ground state of SrSnO_3 becomes Phase-B again at large compressive strain. There is no obvious explanation of this behavior. The transition near 0% in both compounds seem to arise from a preference for a phase with larger rotation angles (most clearly seen on the right panels of Fig. 9), but even the complete irrep decomposition of SrSnO_3 (left panels of Fig. 9, as well as Supplementary Fig. 20, 22) doesn't point to any clues about the energy trends at larger compressive strain.

CaTiO_3 also has the same phase transition around 0% strain, and so we conclude that the presence of two different $Pnma$ -like $P_{21/c}$ phases is a general property of many $Pnma$ perovskites under (111) strain. Additionally, in-line with the stronger ferroelectric tendencies of

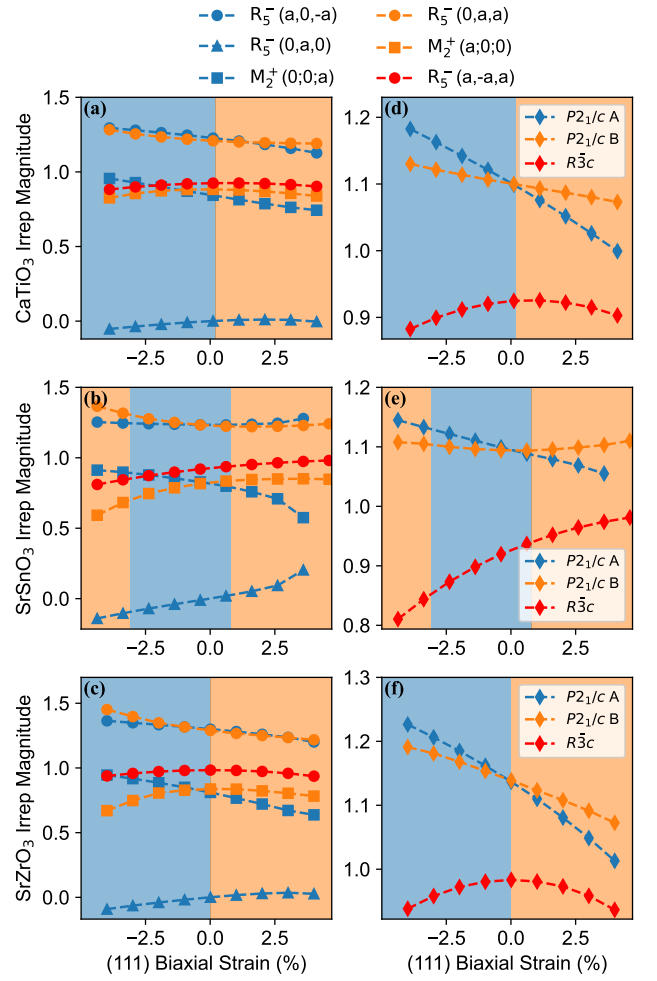


FIG. 9. Octahedral rotation irreps, R_5^- and M_2^+ , of the relevant phases as a function of (111) strain. Panels (a), (b) and (c) show the individual components while panels (d), (e) and (f) show the average rotation magnitude over three axes. The blue, orange and red colors correspond to the irreps of $P_{21/c}$ Phase A, $21/c$ Phase B and $R\bar{3}c$, respectively. The magnitude of the rotation gradually increases when going from tensile to compressive (111) strain. The phase with larger rotation magnitude is generally more stable since it provides better stabilization to the small A -site.

CaTiO_3 discussed earlier, there is another, second-order allowed phase transition at $\sim +1\%$ tensile strain from $P_{21/c}$ Phase B to the predominantly-in-plane polar Pc phase. This phase is again distinct from the polar Pc phase (not shown) obtained from the Phase A of $P_{21/c}$ even though its space group name is the same.

IV. DISCUSSION

There are distinct differences between the phase diagrams of $Pnma$ perovskites under (001) and (111) epitaxial strain. Firstly, there is a larger number of different

Bulk phase	Glazer notation	Symm. modes	(111) strain	Polar phases	(001) strain	Polar phases
$Pm\bar{3}m$	$a^0a^0a^0$		$R\bar{3}m$	$R3m; C2; Cm$	$P4/mmm$	$Pmm2; P4mm; Amm2; Pm; Cm$
$I4/mcm$	$a^0a^0b^-$ $a^-b^0b^0$	R_5^-	$C2/c$	$C2; Cc$	$I4/mcm$ $Fmmm$	$Fmm2; I4cm; Ima2; Cm; Cc$ $Fmm2; Cm$
$Imma$	$a^-a^-b^0$ $a^0b^-b^-$	R_5^-	$C2/c$	$C2; Cc$	$Imma$ $C2/m$	$Cm; Ima2; Imm2; Cc$ $C2; Cm$
$R\bar{3}c$	$a^-a^-a^-$	R_5^-	$R\bar{3}c$	$R3c; C2; Cc$	$C2/c$	$C2; Cc$
$P4/mbm$	$a^0a^0b^+$ $a^+b^0b^0$	M_2^+	$P2_1/c$	$P2_1; Pc$	$P4/mbm$ $Cmmm$	$Amm2; P4bm; Pmc2_1; Pm; Cm; Pc$ $Cmm2; Amm2; Cm; Pm$
$I4/mmm$	$a^+a^+b^0$ $a^0b^+b^+$	M_2^+	$C2/m$	$C2; Cm$	$I4/mmm$ $Immm$	$Imm2; I4mm; Fmm2; Cm$ $Imm2; Cm$
$Im\bar{3}$	$a^+a^+a^+$	M_2^+	$R\bar{3}$	$R3$	$Immm$	$Imm2; Cm$
$C2/m$	$a^0b^-c^-$	R_5^-	$P\bar{1}$		$C2/m$	$C2; Cm$
$C2/c$	$a^-a^-b^-$ $a^-b^-b^-$	R_5^-	$C2/c$	$C2; Cc$	$C2/c$ $P\bar{1}$	$C2; Cc$
$Pnma$	$a^-a^-b^+$ $a^+b^-b^-$	M_2^+, R_5^-	$P2_1/c$	$P2_1; Pc$	$Pnma$ $P2_1/m$	$Pna2_1; Pmc2_1; Pmn2_1; Pm; Pc$ $P2_1; Pm$
$Cmcm$	$a^0b^+c^-$	M_2^+, R_5^-	$P\bar{1}$		$Cmcm$	$Ama2; Cmc2_1; Amm2; Cc; Pm; Cm$
$P4_2/nmc$	$a^+a^+b^-$ $a^-b^+b^+$	M_2^+, R_5^-	$C2/c$	$C2; Cc$	$P4_2/nmc$ $Pmnm$	$Pmn2_1; P4_2mc; Aa2; Pc; Pm; Cc$ $Pmm2; Pmn2_1; Pm; Pc$
$Immm$	$a^+b^+c^+$	M_2^+	$P\bar{1}$		$Immm$	$Imm2; Cm$
$P2_1/m$	$a^+b^-c^-$	M_2^+, R_5^-	$P\bar{1}$		$P2_1/m$	$P2_1; Pm$
$P\bar{1}$	$a^-b^-c^-$	R_5^-	$P\bar{1}$		$P\bar{1}$	

TABLE III. Symmetries of all perovskite phases with different rotation patterns, polarization, and biaxial strain. We list the rotation patterns in Glazer notation, relevant rotation irreps, strained phases and their polar phases obtained under (001) strain (Γ_3^+), (111) strain (Γ_5^+) and polarization along cubic axes (Γ_4^-). Symmetry modes are given with respect to the cubic $Pm\bar{3}m$ structure of ABO_3 perovskite with atomic position given by A (1a), B (1b), and O (3c). The polar structure $P1$ with polarization along a general direction is trivially allowed in each row and hence is not listed.

phases present in the (001) case. This is in part because of the greater richness of the phase space in the (001) case as seen from Table III, which lists the symmetries of all possible structures under (001) and (111) strain. Due to the fact that the axes of the octahedral rotation in $Pnma$ are aligned with a unique crystalline axis (the [001] direction), it can achieve a larger pool of structures with different space groups, by permuting the direction of rotation and strain. The (111) strain applies for all three possible pseudo-cubic directions for octahedral rotations equally, and hence, can only achieve one symmetry configuration for each octahedral rotation pattern. Another reason that helps having fewer distinct phases under (111) strain is the seemingly lower sensitivity of the phonon instabilities to (111) biaxial strain due to strain itself not affecting the lattice vectors as much as (001) strain.

Secondly, $CaTiO_3$ polarizes readily under (001) strain, in both the compressive and tensile region. Under (111), it only polarizes in the tensile region, and only at larger strain magnitude. A similar situation was observed from DFT in $SrTiO_3$ [65] which has weak $a^0a^0c^-$ rotations and becomes polar under tensile (111) strain only, and $BaTiO_3$ [66] which is polar in bulk but becomes centrosymmetric under compressive (111) strain.

V. SUMMARY AND CONCLUSIONS

In this study, we applied first principles DFT to investigate the effect of biaxial strain on (001) and (111)-oriented $Pnma$ perovskites, which constitute more than half of all perovskite oxides [11]. We found that it is essential to relax the monoclinic angles of the out-of-plane vectors while applying the biaxial constraint, especially when monoclinic phases are abundant in the phase diagram, since it plays an important role in stabilizing these phases and hence obtaining the correct ground state structure. Under (111) strain, we found two different structures in the tensile and compressive strain regions, both having $P2_1/c$ symmetry. We also found that $CaTiO_3$ polarizes under small tensile and compressive (001) strain and relatively larger tensile (111) strain. The phase diagram for $CaTiO_3$ under (001) strain is different from previous predictions [64], with no $Pnma$ phase and polarization in the compressive strain region.

We performed an analysis of all distortions with different irreps present in these structures as a function of strain and found that the magnitude of irreps remain relatively stable under (111) strain. For (001) strain, many octahedral rotational modes' amplitudes reduce with increasing tensile strain, and increase with a relatively high rate under compressive strain.

In summary, we compared the effects of two distinct strain directions in biaxial perovskites, and showed that

the (111) strain not only realize symmetries that are not present in (001) strained films, but also the trends of octahedral rotation angles and ferroelectric polarization is very different under (111) strain than it is under (001) strain. Hence, different strain directions is a way to manipulate the crystal structure and obtain new phases of complex oxides. While all compounds we considered are band insulators, these new structural phases' effects on the electronic structure will likely provide many open questions of increasing importance due to the increas-

ing availability of (111) films grown by molecular beam epitaxy or pulsed laser deposition.

ACKNOWLEDGMENTS

This work was supported by the US Department of Energy through the University of Minnesota (UMN) Center for Quantum Materials, under Grant No. DE-SC0016371.

-
- [1] E. G. Moloney, V. Yeddu, and M. I. Saidaminov, Strain engineering in halide perovskites, *ACS Materials Letters* **2**, 1495 (2020).
- [2] D. G. Schlom, L.-Q. Chen, C. J. Fennie, V. Gopalan, D. A. Muller, X. Pan, R. Ramesh, and R. Uecker, Elastic strain engineering of ferroic oxides, *MRS Bulletin* **39**, 118–130 (2014).
- [3] C. Zhu, X. Niu, Y. Fu, N. Li, C. Hu, Y. Chen, X. He, G. Na, P. Liu, H. Zai, *et al.*, Strain engineering in perovskite solar cells and its impacts on carrier dynamics, *Nature communications* **10**, 815 (2019).
- [4] Y. Jiao, S. Yi, H. Wang, B. Li, W. Hao, L. Pan, Y. Shi, X. Li, P. Liu, H. Zhang, *et al.*, Strain engineering of metal halide perovskites on coupling anisotropic behaviors, *Advanced Functional Materials* **31**, 2006243 (2021).
- [5] B. Liu, J. Li, G. Wang, F. Ye, H. Yan, M. Zhang, S.-C. Dong, L. Lu, P. Huang, T. He, *et al.*, Lattice strain modulation toward efficient blue perovskite light-emitting diodes, *Science Advances* **8**, eabq0138 (2022).
- [6] D. Yang and D. Huo, Cation doping and strain engineering of CsPbBr₃-based perovskite light emitting diodes, *Journal of Materials Chemistry C* **8**, 6640 (2020).
- [7] D. Dimos and C. Mueller, Perovskite thin films for high-frequency capacitor applications, *Annual Review of Materials Science* **28**, 397 (1998).
- [8] D. G. Schlom, L. Q. Chen, C. B. Eom, K. M. Rabe, S. K. Streiffer, and J. M. Triscone, Strain tuning of ferroelectric thin films, *Annual Review of Materials Research* **37**, 589 (2007).
- [9] L. W. Martin and A. M. Rappe, Thin-film ferroelectric materials and their applications, *Nature Reviews Materials* **2**, 16087 (2017).
- [10] A. Fernandez, M. Acharya, H. Lee, J. Schimpf, Y. Jiang, D. Lou, Z. Tian, and L. W. Martin, Thin-Film Ferroelectrics, *Advanced Materials* **34**, 1 (2022).
- [11] M. W. Lufaso and P. M. Woodward, Prediction of the crystal structures of perovskites using the software program SPuDS, *Acta Crystallographica Section B: Structural Science* **57**, 725 (2001).
- [12] P. M. Woodward, Octahedral tilting in perovskites. II. structure stabilizing forces, *Acta Crystallographica Section B: Structural Science* **53**, 44 (1997).
- [13] P. M. Woodward, Octahedral tilting in perovskites. i. geometrical considerations, *Acta Crystallographica Section B: Structural Science* **53**, 32 (1997).
- [14] A. M. Glazer, The classification of tilted octahedra in perovskites, *Acta Crystallographica Section B Structural Crystallography and Crystal Chemistry* **28**, 3384 (1972).
- [15] C. J. Howard and H. T. Stokes, Group-theoretical analysis of octahedral tilting in perovskites, *Acta Crystallographica Section B Structural Science* **54**, 782 (1998).
- [16] Z. Wang, D. Gautreau, T. Birol, and R. M. Fernandes, Strain-tunable metamagnetic critical endpoint in mott insulating rare-earth titanates, *Physical Review B* **105**, 10.1103/PhysRevB.105.144404 (2022).
- [17] A. Najev, S. Hameed, D. Gautreau, Z. Wang, J. Joe, M. Požek, T. Birol, R. M. Fernandes, M. Greven, and D. Pelc, Uniaxial strain control of bulk ferromagnetism in rare-earth titanates, *Physical Review Letters* **128**, 10.1103/PhysRevLett.128.167201 (2022).
- [18] A. K. Choquette, C. R. Smith, R. J. Sichel-Tissot, E. J. Moon, M. D. Scafetta, E. D. Gennaro, F. M. Granozio, E. Karapetrova, and S. J. May, Octahedral rotation patterns in strained EuFeO₃ and other Pbnm perovskite films: Implications for hybrid improper ferroelectricity, *Physical Review B* **94**, 10.1103/PhysRevB.94.024105 (2016).
- [19] H. F. Kay and P. C. Bailey, Structure and properties of CaTiO₃, *Acta Crystallographica* **10**, 219 (1957).
- [20] M. D. Biegalski, L. Qiao, Y. Gu, A. Mehta, Q. He, Y. Takamura, A. Borisevich, and L. Q. Chen, Impact of symmetry on the ferroelectric properties of CaTiO₃ thin films, *Applied Physics Letters* **106**, 10.1063/1.4918805 (2015).
- [21] T. Wang, A. Prakash, Y. Dong, T. Truttmann, A. Bucek, R. James, D. D. Fong, J.-W. Kim, P. J. Ryan, H. Zhou, T. Birol, and B. Jalan, Engineering SrSnO₃ phases and electron mobility at room temperature using epitaxial strain, *ACS Applied Materials & Interfaces* **10**, 43802 (2018).
- [22] S. Okamoto, Doped mott insulators in (111) bilayers of perovskite transition-metal oxides with a strong spin-orbit coupling, *Physical Review Letters* **110**, 10.1103/PhysRevLett.110.066403 (2013).
- [23] A. Rüegg and G. A. Fiete, Topological insulators from complex orbital order in transition-metal oxides heterostructures, *Physical Review B* **84**, 201103 (2011).
- [24] S. Chakraverty, A. Ohtomo, M. Okude, K. Ueno, and M. Kawasaki, Epitaxial structure of (001)- and (111)-oriented perovskite ferrate films grown by pulsed-laser deposition, *Crystal Growth and Design* **10**, 1725 (2010).
- [25] Y. Tang, Y. Zhu, X. Ma, Z. Hong, Y. Wang, W. Wang, Y. Xu, Y. Liu, B. Wu, L. Chen, C. Huang, L. Chen, Z. Chen, H. Wu, and S. J. Pennycook, A Coherently Strained Monoclinic [111] PbTiO₃ Film Exhibiting Zero Poisson's Ratio State, *Advanced Functional Materials*

- 29**, 1 (2019).
- [26] Y. Liang, W. Li, S. Zhang, C. Lin, C. Li, Y. Yao, Y. Li, H. Yang, and J. Guo, Homoepitaxial SrTiO₃ (111) Film with High Dielectric Performance and Atomically Well-Defined Surface, *Scientific Reports* **5**, 1 (2015).
- [27] J. Roth, T. Kuznetsova, L. Miao, A. Pogrebnnyakov, N. Alem, and R. Engel-Herbert, Self-regulated growth of [111]-oriented perovskite oxide films using hybrid molecular beam epitaxy, *APL Materials* **9**, 10.1063/5.0040047 (2021).
- [28] S. Middey, P. Rivero, D. Meyers, M. Kareev, X. Liu, Y. Cao, J. W. Freeland, S. Barraza-Lopez, and J. Chakhalian, Polarity compensation in ultra-thin films of complex oxides: The case of a perovskite nickelate, *Scientific Reports* **4**, 10.1038/srep06819 (2014).
- [29] S. Middey, D. Meyers, D. Doennig, M. Kareev, X. Liu, Y. Cao, Z. Yang, J. Shi, L. Gu, P. J. Ryan, R. Pentcheva, J. W. Freeland, and J. Chakhalian, Mott electrons in an artificial graphenelike crystal of rare-earth nickelate, *Physical Review Letters* **116**, 10.1103/PhysRevLett.116.056801 (2016).
- [30] M. Gibert, M. Viret, P. Zubko, N. Jaouen, J. M. Tonnerre, A. Torres-Pardo, S. Catalano, A. Gloter, O. Stéphan, and J. M. Triscone, Interlayer coupling through a dimensionality-induced magnetic state, *Nature Communications* **7**, 10.1038/ncomms11227 (2016).
- [31] J. Kim, M. Yu, J.-W. Lee, S.-L. Shang, G.-Y. Kim, P. Pal, J. Seo, N. Campbell, K. Eom, R. Ramachandran, M. S. Rzchowski, S. H. Oh, S.-Y. Choi, Z.-K. Liu, J. Levy, and C.-B. Eom, Electronic-grade epitaxial (111) KTaO₃ heterostructures (2023), arXiv:2308.13180 [cond-mat.mtrl-sci].
- [32] J. van Roosmalen, P. van Vlaanderen, and E. Cordfunke, On the structure of SrZrO₃, *Journal of Solid State Chemistry* **101**, 59 (1992).
- [33] M. Glerup, K. S. Knight, and F. W. Poulsen, High temperature structural phase transitions in SrSnO₃ perovskite, *Materials Research Bulletin* **40**, 507 (2005).
- [34] M. Yashima and R. Ali, Structural phase transition and octahedral tilting in the calcium titanate perovskite CaTiO₃, *Solid State Ionics* **180**, 120 (2009).
- [35] B. J. Kennedy, C. J. Howard, and B. C. Chakoumakos, High-temperature phase transitions in SrZrO₃, *Physical Review B* **59**, 4023 (1999).
- [36] G. Kresse and J. Furthmüller, Efficiency of ab-initio total energy calculations for metals and semiconductors using a plane-wave basis set, *Computational Materials Science* **6**, 15 (1996).
- [37] G. Kresse and J. Furthmüller, Efficient iterative schemes for ab initio total-energy calculations using a plane-wave basis set, *Phys. Rev. B* **54**, 11169 (1996).
- [38] P. E. Blöchl, Projector augmented-wave method, *Physical review B* **50**, 17953 (1994).
- [39] J. P. Perdew, A. Ruzsinszky, G. I. Csonka, O. A. Vydrov, G. E. Scuseria, L. A. Constantin, X. Zhou, and K. Burke, Restoring the density-gradient expansion for exchange in solids and surfaces, *Phys. Rev. Lett.* **100**, 136406 (2008).
- [40] H. T. Stokes, D. M. Hatch, and B. J. Campbell, FINDSYM, ISOTROPY Software Suite, iso.byu.edu., <https://stokes.byu.edu/iso/findsym.php> (), accessed: 2023-06-01.
- [41] H. T. Stokes and D. M. Hatch, Findsymb: program for identifying the space-group symmetry of a crystal, *Journal of Applied Crystallography* **38**, 237 (2005).
- [42] H. T. Stokes, D. M. Hatch, and B. J. Campbell, ISODISTORT, ISOTROPY Software Suite, iso.byu.edu., <https://stokes.byu.edu/iso/isodistort.php> (), accessed: 2023-06-01.
- [43] B. J. Campbell, H. T. Stokes, D. E. Tanner, and D. M. Hatch, *ISODISPLACE*: a web-based tool for exploring structural distortions, *Journal of Applied Crystallography* **39**, 607 (2006).
- [44] H. T. Stokes, D. M. Hatch, and B. J. Campbell, INVARIANTS, ISOTROPY Software Suite, iso.byu.edu., <https://stokes.byu.edu/iso/invariants.php> (), accessed: 2023-07-01.
- [45] D. M. Hatch and H. T. Stokes, *INVARIANTS*: program for obtaining a list of invariant polynomials of the order-parameter components associated with irreducible representations of a space group, *Journal of Applied Crystallography* **36**, 951 (2003).
- [46] M. I. Aroyo, J. M. Perez-Mato, D. Orobengoa, E. Tasci, G. de la Flor, and A. Kirov, Crystallography online: Bilbao crystallographic server, *Bulg. Chem. Commun* **43**, 183 (2011).
- [47] K. Momma and F. Izumi, Vesta 3 for three-dimensional visualization of crystal, volumetric and morphology data, *Journal of applied crystallography* **44**, 1272 (2011).
- [48] A. Togo and I. Tanaka, First principles phonon calculations in materials science, *Scripta Materialia* **108**, 1 (2015).
- [49] H. J. Monkhorst and J. D. Pack, Special points for brillouin-zone integrations, *Phys. Rev. B* **13**, 5188 (1976).
- [50] A. T. Mulder, N. A. Benedek, J. M. Rondinelli, and C. J. Fennie, Turning ABO₃ Antiferroelectrics into Ferroelectrics: Design Rules for Practical Rotation-Driven Ferroelectricity in Double Perovskites and A₃B₂O₇ Ruddlesden-Popper Compounds, *Advanced Functional Materials* **23**, 4810 (2013).
- [51] S. Li and T. Birol, Free-carrier-induced ferroelectricity in layered perovskites, *Phys. Rev. Lett.* **127**, 087601 (2021).
- [52] See the supplementary information for details.
- [53] Y. Zhang, J. Wang, M. P. K. Sahoo, T. Shimada, and T. Kitamura, Strain-induced ferroelectricity and lattice coupling in BaSnO₃ and SrSnO₃, *Physical Chemistry Chemical Physics* **19**, 26047 (2017).
- [54] I. Bersuker, On the origin of ferroelectricity in perovskite-type crystals, *Physics Letters* **20**, 589 (1966).
- [55] R. Cohen and H. Krakauer, Lattice dynamics and origin of ferroelectricity in BaTiO₃: Linearized-augmented-plane-wave total-energy calculations, *Physical Review B* **42**, 6416 (1990).
- [56] N. A. Benedek and T. Birol, ‘ferroelectric’ metals reexamined: fundamental mechanisms and design considerations for new materials, *Journal of Materials Chemistry C* **4**, 4000 (2016).
- [57] First-principles study of structural and vibrational properties of SrZrO₃, *Physical Review B* **85**, 064112 (2012).
- [58] J. H. Haeni, P. Irvin, W. Chang, R. Uecker, P. Reiche, Y. L. Li, S. Choudhury, W. Tian, M. E. Hawley, B. Craigo, A. K. Tagantsev, X. Q. Pan, S. K. Streiffer, L. Q. Chen, S. W. Kirchoefer, J. Levy, and D. G. Schlom, Room-temperature ferroelectricity in strained strtio₃, *Nature* **430**, 758 (2004).
- [59] C. J. Fennie and K. M. Rabe, Magnetic and electric phase control in epitaxial eutio₃ from first principles, *Physical Review Letters* **97**, 1 (2006).

- [60] J. H. Lee, L. Fang, E. Vlahos, X. Ke, Y. W. Jung, L. F. Kourkoutis, J.-W. Kim, P. J. Ryan, T. Heeg, M. Roeckherath, V. Goian, M. Bernhagen, R. Uecker, P. C. Hammel, K. M. Rabe, S. Kamba, J. Schubert, J. W. Freeland, D. A. Muller, C. J. Fennie, P. Schiffer, V. Gopalan, E. Johnston-Halperin, and D. G. Schlom, A strong ferroelectric ferromagnet created by means of spin–lattice coupling, *Nature* **466**, 954 (2010).
- [61] T. Birol, N. A. Benedek, and C. J. Fennie, Interface control of emergent ferroic order in ruddlesden-popple SrTiO_3 , *Physical Review Letters* **107**, 257602 (2011).
- [62] C.-H. H. Lee, N. D. Orloff, T. Birol, Y. Zhu, V. Goian, E. Roca, R. Haislmaier, E. Vlahos, J. A. Mundy, L. F. Kourkoutis, Y. Nie, M. D. Biegalski, J. Zhang, M. Bernhagen, N. A. Benedek, Y. Kim, J. D. Brock, R. Uecker, X. X. Xi, V. Gopalan, D. Nuzhnyy, S. Kamba, D. A. Muller, I. Takeuchi, J. C. Booth, C. J. Fennie, and D. G. Schlom, Exploiting dimensionality and defect mitigation to create tunable microwave dielectrics, *Nature* **502**, 532 (2013).
- [63] R. C. Haislmaier, Y. Lu, J. Lapano, H. Zhou, N. Alem, S. B. Sinnott, R. Engel-Herbert, and V. Gopalan, Large tetragonality and room temperature ferroelectricity in compressively strained CaTiO_3 thin films, *APL Materials* **7**, 10.1063/1.5090798 (2019).
- [64] C.-J. Eklund, C. J. Fennie, and K. M. Rabe, Strain-induced ferroelectricity in orthorhombic CaTiO_3 from first principles, *Phys. Rev. B* **79**, 220101 (2009).
- [65] S. E. Reyes-Lillo, K. M. Rabe, and J. B. Neaton, Ferroelectricity in [111]-oriented epitaxially strained SrTiO_3 from first principles, *Physical Review Materials* **3**, 030601 (2019).
- [66] R. Oja, K. Johnston, J. Frantti, and R. M. Nieminen, Computational study of (111) epitaxially strained ferroelectric perovskites BaTiO_3 and PbTiO_3 , *Physical Review B* **78**, 094102 (2008).